The role of active mRNA-ribosome dynamics and closing constriction in daughter chromosome separation in *Escherichia coli*

Chathuddasie I. Amarasinghe[1], Mu-Hung Chang[1], Jaana Männik[1], Scott T. Retterer[2], Maxim O. Lavrentovich*[1,3], Jaan Männik*[1]

[1]Department of Physics and Astronomy, University of Tennessee, Knoxville, TN, USA,

[2]Center for Nanophase Materials Sciences, Oak Ridge National Laboratory, Oak Ridge, TN, USA,

[3]Department of Earth, Environment, and Physics, Worcester State University, Worcester, MA, USA.

Correspondence: mlavrent@utk.edu, jmannik@utk.edu

Abstract

The mechanisms by which two sister chromosomes separate and partition into daughter cells in bacteria remain poorly understood. A recent theoretical model has proposed that out-of-equilibrium processes associated with mRNA–ribosome (polysome) dynamics play a significant role in this process. Here we investigate the role of ribosomal dynamics on nucleoid segregation and separation in *Escherichia coli* using high-throughput fluorescence microscopy in microfluidic devices. We compare our experimental observations with predictions from a reaction-diffusion model that includes the interactions among ribosomal subunits, polysomes, and chromosomal DNA. Our results show that the non-equilibrium behavior of mRNA and ribosomes causes them to aggregate at the midcell and this process contributes to the separation of the two daughter chromosomes. However, this effect is considerably weaker than that predicted by the model. Rather than relying solely on active mRNA–ribosome dynamics, our data suggest that the closing division septum via steric interactions and potentially entropic forces between two DNA strands coupled to cell elongation act as additional mechanisms to ensure faithful partitioning of the nucleoids to two daughter cells.

Significance

The mitotic spindle separates chromosomes in eukaryotic cells, but bacteria lack this structure. It remains unclear how bacterial chromosomes partition prior to cell division. It has been hypothesized that non-equilibrium dynamics of polysomes, that is mRNA–ribosome complexes, actively drive the separation of bacterial chromosomes. Using quantitative microscopy combined with computational modeling, we show that polysome dynamics significantly contribute to chromosome segregation in *Escherichia coli* but this process does not constitute the sole mechanism. Our findings suggest the closing division septum via steric interactions and potentially entropic forces between two DNA strands act as additional mechanisms.

Introduction

Chromosome replication and segregation are essential processes in the life cycle of a cell (1-3). Segregation can be divided into two stages: the individualization of daughter chromosomes, and their further separation, which enables their partitioning into daughter cells during cytokinesis (4). Completion of both stages is required for the successful propagation of cells from one generation to the next.

In bacteria, the individualization stage, commonly referred to as DNA segregation, occurs for the most part concurrently with DNA replication (5). In *Escherichia coli*, the newly synthesized DNA loci near *oriC* begin to separate from each other with some delay after initiation of DNA replication (6). After this initial cohesion phase, the sister loci segregate from each other sequentially in the order in which they appear in the genome (7-9). Despite extensive previous research, the underlying molecular mechanism driving the segregation phase in bacteria remains poorly understood (2,3,10). Several active mechanisms for chromosome segregation have been investigated, including ParAB (ParA-ParB-*parS*) (2,10) and homologous Spo0J-Soj system (11), but these are missing in many bacterial species, including *E. coli* (12,13). In addition to the Par-systems, structural maintenance of chromosomes (SMC) proteins, encoded by MukBEF in *E. coli*, have also been implicated in the active segregation (14,15). SMC involvement in segregation is postulated to occur via a successive condensation of DNA around *oriC* via loop extrusion and repulsion of condensed DNA masses away from each other due to excluded volume interactions and chain entropy (14,15). While this is a plausible scenario, MukBEF is not essential for DNA segregation in *E. coli*, except possibly at the fastest growth rates when multifork replication is present (16).

Rather than relying on dedicated protein machinery for segregation, which would expend energy through ATP hydrolysis, it is plausible that the free energy needed for the segregation of chromosomal DNA is derived mostly from the replication process itself. Replication creates two newly formed proximal DNA strands, which, according to polymer physics, experience a repulsive entropic force in confined conditions (17,18). This scenario has been supported by numerous computer simulations (19-26) but it has yet to be experimentally validated. However, the driving force from this so-called entropic mechanism vanishes once the spatial overlap between the two nucleoids becomes zero (26). Therefore, if only the entropic mechanism were present, the two individualized and segregated nucleoids would remain in contact rather than fully separating from each other. The entropic mechanism can, thus, explain the segregation but not the separation phase of the two nucleoids.

The question then arises: what drives chromosomes apart during the separation stage? In eukaryotes the separation is carried out by the mitotic spindle, but no spindles are known to exist in bacteria. DNA translocase FtsK, which is a part of the bacterial cell division apparatus (divisome) (27-29) could be involved in this process (28). However, cells with inactivated FtsK (FtsK K997A) (30) appear to separate their nucleoids and partition them into two daughter cell compartments in the majority of cells (31).

57 Evidence for a different mechanism for separation was revealed by Wu *et al.* (32). These authors observed
58 that in filamentous cells (more than 10 μm) with two nonreplicating nucleoids, the nucleoids separated from
59 each other over large distances so that their centers stayed close to the cell's ¼ positions (32). Wu *et al.*
60 explained such positioning by osmotic pressure from the accumulation of macromolecular crowders, but
61 their explanation relied on the assumption that these crowders are produced in a specific way outside the
62 two nucleoids (32). An alternative explanation, which did not rely on this assumption, was proposed by
63 Miangolarra *et al.* (33). These authors developed a model that included reactions between chromosomal
64 DNA, mRNA, ribosomal subunits and polyribosomes (polysomes), along with their diffusion within the cell.
65 This reaction-diffusion model, which we refer to as the active mRNA-ribosome dynamics model, included
66 reactions for mRNA synthesis, ribosome assembly and disassembly on mRNA, and mRNA degradation.
67 The diffusion of these species was affected by the steric (excluded volume) interactions between these
68 molecules. The model predicted that due to these interactions, the 30S and 50S ribosomal subunits can
69 relatively unhindered diffuse into the nucleoid region, consistent with single-molecule tracking experiments
70 (34,35), while 70S ribosomes, which are further assembled into polyribosomes (polysomes), cannot. The
71 key insight from the model was a finding that an active mRNA synthesis within the nucleoid and the
72 assembly of 30S and 50S ribosomal subunits into polysomes around these mRNAs create instability within
73 the nucleoid. This instability drives the nucleoid apart into two distinct nucleoid lobes at some critical cell
74 length (33). The model also predicted that the two daughter nucleoid centers would position at the quarter
75 points of the cell once the transition occurred and stay in these locations even when cells filamented,
76 consistent with the experimental observations by Wu *et al*. (32).

77 Here, we investigate the mechanisms that individualize chromosomes in the late stages of segregation and
78 drive their separation in normal growth conditions. In particular, we test the active mRNA-ribosome
79 dynamics model by Miangolarra *et al.* in non-filamenting cells growing in slow-growth conditions with simple
80 DNA topology. To this end, we use high-throughput microscopy in microfluidic devices to determine the
81 distributions of ribosomes, nucleoids, and replication machinery during cell and replication cycles. We
82 quantitatively compare the acquired experimental data to our own reaction-diffusion model, which is
83 conceptually similar to the one proposed by Miangolarra *et al*. (33). We first find that the termination of DNA
84 replication does not have a significant effect on the nucleoid segregation dynamics. Instead, DNA expands
85 and daughter nucleoids separate in proportion to cell length increase during this stage of the cell cycle. Our
86 data, when compared to the model, supports the idea that active ribosome dynamics facilitates separation
87 of two nucleoids in normal growth conditions. However, in cells where active ribosome dynamics are halted,
88 we observe that the separation of daughter nucleoids still increases proportionally with cell length. In
89 addition to this effect, we identify closing constriction, as a new mechanism, that has a significant effect in
90 separating the two daughter nucleoids and partitioning them into two daughter cells. Based on this
91 evidence, we propose a multi-process model to explain the nucleoid segregation and separation dynamics
92 in *E. coli*.

Results

The midcell DNA density minimum evolves independent of replication termination

DNA segregation cannot occur without DNA being first replicated. We first hypothesized that the progression of segregation is directly driven by the replication stage. In previous works on the segregation of nucleoids using tracking of fluorescently labeled loci in the chromosome (5,6,9,36,37), following bulk segregation (25,38), or labeling the replication terminus by MatP fusion (25,39), the segregation process had not been directly tracked during the replication cycle at the single cell level. To do so now, we labeled the beta-clamp protein, DnaN, with fluorescent fusion (Ypet-DnaN) (40). To follow the dynamics of the whole chromosome, we used HupA-mCherry, which has been tested before and is known to bind uniformly throughout the chromosome (41). We chose to carry out measurements in slow growth conditions where, at most, only a single replication cycle is ongoing (42) and where we could accurately determine timings for the initiation and termination of the replication (SI Fig. S1). We imaged cells in mother machine microfluidic devices (43,44), obtaining about 30-50 time points per cell cycle from several hundred cells. We averaged these data over the cell population and produced kymographs (Fig. 1A-B).

To characterize the segregation process, we determined the total extent of all nucleoids in the cell, $L_{nuc,ext}$, and the sum of nucleoid lengths, $L_{nuc,sum}$ (Fig. 1C; for details, see Materials and Methods). These measurements showed that the outer edges of the nucleoids, as determined by $L_{nuc,ext}$, stayed at about a constant distance (0.5/2 μm ≈ 0.25 μm) from the cell ends throughout the replication cycle (Fig. 1C). Notably, the total extent and the sum of nucleoid lengths did not show any discontinuities at the termination of replication (Fig. 1C). To further verify this unexpected result, we aligned the curves from individual cells relative to replication termination time, Trt , but still found only smooth continuous changes (SI Fig. S2). We also found a comparable cell-cycle independent distance throughout the division cycle in both slow (SI Fig. S3) and moderately fast growth conditions (SI Fig. S4). The measured exclusion distance of nucleoids from poles (0.25 μm) is slightly less than the length of the hemispherical cap region (0.3-0.35 μm) (45) . Therefore, the chromosomal DNA is mostly excluded from the polar caps. The data furthermore show that instead of nucleoid elongation and separation being controlled by the replication cycle, the length of individual nucleoids, $L_{nuc,sum}$, and their total extent in the cell, $L_{nuc,ext}$, increases in proportion to cell length. This dependence has also been noticed in some earlier studies (25,32,46), although the replication period was not directly determined in these works.

In addition to $L_{nuc,sum}$ and $L_{nuc,ext}$, we also determined the DNA density at midcell during the replication cycle as a different measure of DNA segregation and separation (Fig. 1D). In the early stages of replication, there was a maximum DNA density at midcell (Fig. 1A). Upon completion of about 60% of the replication cycle, the DNA amount at the midcell started to decrease (Fig.1D). This decrease corresponded to the formation of a local DNA density minimum (Fig. 1E). As with our other nucleoid measurements, the midcell minimum continued to decline further after replication termination without any distinct changes. Altogether,

these results, combined with the nucleoid length measurements, indicate that while chromosome replication is a prerequisite for segregation, nucleoid segregation is not strongly driven by the replication process itself at late stages of the replication cycle. Instead, separation of two nucleoids follows overall cell growth.

Correlated and anti-correlated periods of DNA and ribosome density distributions during the cell cycle

In balanced growth, cells size increases proportional to its ribosome number. We hypothesized that the DNA segregation at late stages of the replication cycle could be driven by active ribosome dynamics that involve mRNA synthesis and degradation and are associated with the assembly and disassembly of polyribosomes (33). To test this hypothesis, we constructed a strain where the nucleoids were labeled with HupA-mYpet fluorescent marker (25,41) and ribosomes with RpsB-mCherry (47,48) (for details, see Materials and Methods). Both labels had been tested in previous studies (25,41,47,48). Since this strain lacked a marker for replication, we followed nucleoid segregation and ribosome accumulations throughout the division cycle (Fig. 2A-C), which we customarily refer to as the cell cycle.

In the first half of the cell cycle, the population-averaged data shows a unimodal distribution of DNA with a maximum close to the cell center (Fig. 2D, Age 0.10, 0.30). Notably, the ribosome density distribution is similar to the DNA density distribution from the same cells, showing a broad density maximum at the midcell. The co-localization of the two distribution maxima appears not consistent with equilibrium thermodynamic models (49,50), where ribosomes phase separate from DNA rich regions. Note that there are no local maxima in the ribosome density at cell poles in distributions in Fig. 2D. The excess ribosome density at cell poles is not expected to result in maxima in the extreme ends of 1D density distributions, which are projections of the 3D density onto the long axis of the cell. The maxima are missing because of the rounded shape of the poles and diffraction-limited imaging. As the cell cycle progresses, the nucleoid expands, and the population-average DNA density distribution becomes bimodal (bilobed (6)) with a local minimum near its center (Fig.2D, Age=0.50). This minimum is accompanied by the sharper ribosome density maximum at the same location. In this case, the observed anti-correlated densities of ribosomes and chromosomal DNA at the midcell are consistent with the phase separation of nucleoid and ribosomes, as expected from equilibrium thermodynamics (49,50). This excess ribosome density increases as the cell cycle progresses, and the DNA density at midcell decreases (Fig. 2D, Age=0.50, 0.70). At the end of the cell cycle, the ribosome density, instead of further increasing, decreases while the DNA density continues also to decrease (Fig. 2D, Age=0.90). This positively correlated behavior again cannot be explained by equilibrium considerations of volume exclusion between ribosomes and chromosomes.

To determine the timing of these behaviors, we plot the Pearson correlation coefficient, R, between the DNA and ribosome distributions along the long axis of the cell as a function of cell cycle age, expressed as the fraction of completed cell cycle (Fig. 2E). At the beginning of the cell cycle, the two distributions show small but positive R values, as expected based on the coincidence of their maxima. At about cell age 0.5, the

163 correlation coefficient starts to decrease and becomes negative. This decrease in R corresponds to a
164 concurrent decrease in DNA and an increase in ribosome amounts at midcell (Fig. 2F). The correlation
165 coefficient reaches its minimum at cell age ~0.75, then starts to increase and becomes positive by the end
166 of the cell cycle. At cell cycle age ~0.75, the midcell ribosome numbers reach their peak and start to
167 decrease thereafter, while the amount of DNA at midcell continues to decrease until the end of the cell cycle
168 (Fig. 2F). To understand the cause of the decrease in ribosome numbers at midcell at the end of the cell
169 cycle, we compare these data with the midcell phase contrast signal from the same cells (Fig. 2F, black
170 line). There is an upturn in the phase contrast signal at the time when the ribosome numbers peaked. The
171 increase in the phase contrast signal signifies the onset of constriction (51). The midcell ribosome numbers,
172 thus, start to decrease as the cell starts to constrict in this region.

173 Based on traces in Fig. 2D the excess fraction of ribosomes in the midcell appeared small throughout the
174 cell cycle. To quantify this fraction, we decompose the ribosomal density distribution into a midcell fraction
175 and a uniform background by fitting the data from individual cells (see Materials and Methods). We find that
176 the population average excess fraction of ribosomes is only 4% of the cell total at its peak at cell age ~0.75
177 (Fig. 2G). At the same time, the excess fraction before the DNA density minimum at midcell begins to form
178 is 2.5%. The equilibrium thermodynamics can qualitatively explain the increase in the excess fraction from
179 2.5% to 4%. However, it fails to explain the 2.5% fraction present in the early cell cycle.

180 To verify the validity of the above findings, we constructed a strain in which the fluorescent mCherry fusion
181 was added to the C-terminus of the 50S ribosomal protein RplI (RplI-mCherry) instead of labeling the 30S
182 subunit (SI Fig. S5A-C). This label has also been previously characterized and tested (51). The cells with
183 RplI-mCherry label showed the same behavior as the one with RpsB-mCherry (SI Fig. S5D-G), including
184 co-localization of ribosome and DNA density distributions at the midcell at early cell cycle (SI Fig. S5D,
185 Age=0.15) and comparably small excess fraction of ribosomes at midcell at its peak value (3.5%) (SI Fig.
186 S5G).

187 We also investigated whether the same behaviors would occur in faster growth rates in M9 glucose + CAS
188 medium (SI Fig. S6). Under this growth condition, the replication cycle initiates predominantly in the
189 previous cell cycle and completes at the early cell cycle (42). Accordingly, a minimum in the nucleoid density
190 distribution is already observed at the midcell at cell birth (SI Fig. S6C). Consequently, unlike in slow growth
191 conditions, there is no positive correlation between DNA and ribosome density distribution during the early
192 stages of the cell cycle (SI Fig. S6D). Aside from this difference, the other behaviors (SI Fig. S6E-F),
193 including a small excess ribosome fraction at the cell center at its peak value (5.5%), are consistent with
194 those observed under slower growth conditions.

195

196 **The DNA and ribosome correlation patterns in the early and midcell cycle are qualitatively explained**
197 **by the coupled DNA and ribosome dynamics model**

198 To understand if the observed ribosome and nucleoid localization patterns can be explained by the active
199 dynamics of mRNA and ribosomes, we developed our own reaction-diffusion model (see Methods, *The*
200 *Coupled DNA and Ribosome Dynamics Model*). We then compared the calculated cell cycle-dependent
201 DNA and ribosome densities from the model to the experimental data. Our 1D model is similar to the one
202 developed by Miangalorra *et al*. (33), considering mRNA synthesis and degradation, as well as the
203 assembly of polysomes (polyribosomes) from ribosomal subunits. Polysome and ribosomal subunits
204 interact with each other and with DNA via excluded volume interactions. However, unlike the previously
205 published model, ours uses a power-law term (50,52) instead of a virial expansion to describe DNA and
206 polysome self-interactions. Additionally, our model does not explicitly simulate bare mRNA and polysomes
207 of varying sizes; instead, it considers only an average-sized polysome. Unlike the previous model (33), ours
208 also includes cell growth, assuming DNA and ribosome amounts increase with cell length (or volume).

209 To qualitatively compare the model to experimental data, we plotted the nucleoid and ribosome density
210 distribution along the cell length at different cell cycle times (Fig. 2H, SI Fig. S7A-B). These times were
211 selected to be comparable, though not identical to those shown in Fig. 2D. Notably, the ribosome distribution
212 predicted by the model shows a small local maximum at the cell middle, coinciding with the maximum of
213 the nucleoid distribution at the early stages of the cell cycle (Fig. 2H, Age 0.10, 0.30). This is consistent with
214 experimental data (Fig. 2D, Age 0.15). In the model, the midcell maximum in ribosome distribution arises
215 at the start of the cell cycle. This occurs because 30S and 50S ribosomal subunits can diffuse almost
216 unhindered into the nucleoid region, where they assemble into polysomes. Since the rate of polysome
217 formation is proportional to DNA density in the model, the maxima of ribosome and DNA densities coincide.

218 The model predicts that excess ribosome density at the midcell cleaves the initial single nucleoid into two
219 nucleoid masses at some critical cell length due to excluded volume interactions (Fig 2H, Age=0.32). After
220 this transition, ribosome and DNA density distributions become anti-correlated (Fig 2H, Age=0.72; SI Fig.
221 S7C), which is consistent with experimental observations. Separation of the two DNA masses in the model
222 occurs rapidly, within 5% (0.05) of the cell cycle. During this transition, the excess fraction of ribosomes at
223 midcell reaches 48% and approximately maintains this value for the rest of the cycle (SI Fig. S7D). In
224 contrast, the experiment shows that the fraction reaches only 4.5% (Fig. 2G). The model thus correctly
225 predicts a local maximum in ribosome density at the cell middle in the early stages. However, it shows a
226 significantly higher accumulation of ribosomes in the cell middle in the later stages of the cell cycle
227 compared to the experimental data. We hypothesized that the substantially higher ribosome fractions
228 observed in the model are due to its 1D nature. In a 3D cell, ribosomes could form an outer shell around
229 the nucleoid, as has been proposed by earlier single-molecule tracking experiments of ribosomes (34).
230 Since this shell could not be derived from our 1D model, we added its effect *ad hoc* to our model (SI Fig.
231 S8A-B). Additionally, we assumed a uniform ribosome volume density in the shell that matches the density

232 predicted by the 1D model at the cell poles (see *The Concentric Shell Model* in Material and Methods for
233 details). With this addition, the experimental (Fig. 2D) and modeling densities (Fig. 2I) showed similar values
234 with the model yielding about 3% excess of ribosomes at midcell at its peak (SI Fig. S8E). However, to
235 reach this agreement, the inner radius of the added shell needed to be 50% of the cell radius while it has
236 been estimated based on single-molecule tracking experiments that the inner radius is about 80% of the
237 cell's radius (34). These comparisons suggest that the coupled DNA and ribosome dynamics model could
238 better explain the data if it were implemented in 3D.

239 **Constriction pushes aside daughter nucleoids**

240 In the late stages of the cell cycle, when a constriction forms at the midcell, the model and experimental
241 data do not agree with each other. The data reveals a decreasing ribosome fraction at the midcell (Fig. 2G),
242 whereas the model maintains almost a constant fraction (SI Fig. S7E). We hypothesized that the closing
243 constriction pushes aside the ribosomes and potentially also the nucleoids. To test this, we carried out
244 experiments in which constriction formation was inhibited by the beta-lactam antibiotic cephalexin. It is well
245 known that despite the inhibition of constriction, cephalexin-treated cells continue to grow in volume and
246 replicate DNA at the same rates as untreated cells (53). We then compared the changes in ribosome and
247 DNA densities between the cephalexin-treated and untreated cells. Since cephalexin prevents cell division,
248 cell age cannot be used to track the progression of DNA and ribosome densities, as done in the previous
249 measurements in Fig. 2. Instead, we determined the timing for the first appearance of the local DNA density
250 minimum at the cell center, T_{min}, following the procedure defined earlier (42) (for details see Materials and
251 Methods). We then aligned the time-dependent data relative to this time (Fig. 3A, B) processing the data
252 from untreated cells the same way (SI Fig. S9A-B). At T_{min}, both the treated and untreated cells show an
253 increase in midcell ribosome numbers (Fig. 3C) and a simultaneous decrease in the midcell DNA amount
254 (Fig. 3D), consistent with the excluded volume interactions between ribosomes and DNA. However, at later
255 times ($time - T_{ab} > 50$ min), the midcell ribosome numbers stay constant in treated cells, while they
256 decrease in untreated ones (Fig. 2C). This comparison confirms that the decrease in ribosome numbers in
257 untreated cells is caused by the closing constriction as we hypothesized.
258
259 The data also indicate that, in addition to reducing the number of ribosomes at midcell, the constriction
260 affects the separation of two daughter nucleoids. Comparison of DNA density at the midcell reveals a clear
261 decrease in DNA in untreated cells relative to treated ones for $time - T_{ab} > 50$ min (Fig. 3D). The effect of
262 constriction is also noticeable in the measured distance between two nucleoid lobes increasing more
263 significantly in untreated cells than in treated ones (Fig. 3E). Altogether, these data show that the closing
264 constriction separates two chromosomes in the late stages of the cell cycle. The effect is not caused by
265 FtsK, since FtsK is recruited to the divisome in both cephalexin-treated and untreated cells (54). The
266 constriction-driven separation appears, thus, to be a steric effect: the closing constriction physically pushes
267 aside the daughter nucleoids.

268 In untreated cells in slow growth conditions, the onset of constriction occurs effectively at the time of the
269 DNA density minimum, T_{min} (42). Therefore, the effects arising from the active ribosome dynamics and
270 constriction on the separation of two daughter nucleoids are overlayed for $time > T_{\min}$. However, the data
271 from cephalexin-treated cells allows us to quantitatively compare the coupled dynamics of DNA and
272 ribosome separation with our model (for $time > T_{\min}$). The DNA and ribosome density distributions
273 predicted by the model (Fig. 3F,G) are qualitatively similar to the experimental data from cephalexin-treated
274 cells (Fig. 3A,B). In quantitative comparisons, the model reproduced some trends in the experimental data
275 but missed others. The model quantitatively correctly predicts the distance between the peaks of two
276 nucleoid lobes (Fig. 3H), but fails to predict the time-dependent decrease in the amount of DNA at midcell
277 (Fig. 3I). In the experiments, the DNA amount changes only 10% over 60 min, while in the model it changes
278 50% within about 5 min. However, after this initial 5 min period, the model and experiment show comparable
279 rates of DNA density decrease at the midcell (Fig. 3I). The reason for the ten-fold slower segregation
280 dynamics observed in the experiments could be related to the choice of model parameters. Reducing the
281 diffusion coefficient of DNA 10-fold considerably slowed down the rate of the change in DNA amount at the
282 midcell, although the cell cycle time for the transition for DNA density from high to low values shifted to later
283 times (SI Fig. S10).
284
285 The experimental data show that after an initial increase at T_{min} , both the excess midcell ribosome fraction
286 (Fig. 3J) and the width of the excess ribosome distribution at midcell (Fig. 3K) remain nearly constant in
287 cephalexin-treated cells. The reasons behind this steady behavior are not intuitively clear, given that the
288 total ribosome number continues to rise as cells elongate. Notably, the model qualitatively reproduces these
289 observed trends but does not accurately predict their numerical values. The quantitative discrepancy for
290 the excess mid cell ribosome fraction (Fig. 3J) can potentially be resolved by including an *ad hoc* concentric
291 ribosome shell around the nucleoid, as previously suggested. Additionally, the experimentally measured
292 width of the ribosome distribution at midcell (Fig. 3K) is approximately three times greater than predicted
293 by the model. This discrepancy likely arises from uncertainties in the chosen Cahn–Hilliard parameters (κ),
294 for which no independent experimental measurements are yet available. Altogether, the model shows
295 qualitative agreement with the experimental data. Its quantitative accuracy could be potentially improved
296 by extending the model to three dimensions and refining its unknown parameters through additional
297 experiments and optimization.

298 **The effect of disruption of polysome formation on nucleoid separation**

299 To perturbatively test the effects of active ribosome dynamics on the separation of two nucleoids, we treated
300 *E. coli* cells with a lethal concentration of rifampicin (300 μg/ml), which inhibits the initiation of RNA synthesis
301 (55). As in the previous measurements, we also added cephalexin to the culture medium at the same time
302 as rifampicin to prevent cells from constricting. Since rifampicin inhibits RNA synthesis, no new polysomes
303 can form after the drug reaches the cells. The existing transcripts can still complete, but this occurs on the

304 time scale of tens of seconds for a single gene and about a minute for longer operons. These timescales
305 are much shorter than our measurement frame rate (4 min). On a slightly longer time scale (3-5 min (56)),
306 the existing polysomes disassemble as their associated mRNAs degrade, releasing ribosomal subunits.

307 To understand the effects arising from these processes, we compared data from cells treated
308 simultaneously with rifampicin and cephalexin (Fig. 4A–C) to cells treated only with cephalexin (Fig. 4D–
309 F). In this comparison, we align the time-dependent data to the antibiotic treatment start time, T_{ab}, instead
310 of T_{min} because most Rif-treated cells lack a detectable midcell DNA density minimum. Additionally, we
311 excluded from the analysis cells with visible constriction at the start of the treatment. As expected, the
312 localized accumulation of ribosomes at the midcell disappears following rifampicin treatment (Fig. 4B, C)
313 due to polysome dissociation and subsequent diffusion of free ribosomal subunits onto the nucleoid region.

314 Following rifampicin addition, the midcell DNA density minimum almost immediately ceases to deepen,
315 although it persists rather than disappearing (Fig. 4G). If steric interactions between DNA and polysomes
316 alone were responsible for creating this minimum, we would expect its complete disappearance on a
317 timescale comparable to polysome dissociation. In contrast, cephalexin-only treated cells continue to show
318 a gradual decrease in midcell DNA density (Fig. 4G). This difference between treatment conditions indicates
319 that active mRNA-ribosome dynamics contribute significantly to establishing the midcell DNA density
320 minimum but are not solely responsible.

321 We next examined nucleoid segregation by measuring the distance between nucleoid centers ($\mathrm{D_{peak}}$) in
322 rifampicin-treated cells (Fig. 4H, SI Fig. S11A). This distance continues to increase for approximately 50
323 minutes, long after active ribosome dynamics ceases (within minutes of rifampicin addition) and polysomes
324 dissociate (3–5 min). Under normal growth conditions, nucleoids separate proportionally to cell elongation
325 (Fig. 1C). To determine if a similar relationship exists following rifampicin treatment, we compared nucleoid
326 center distances to cell length increases, normalizing both metrics at the time of antibiotic addition (Fig. 4H,
327 SI Fig. S11). Indeed, even without active ribosome dynamics, nucleoid centers continue separating
328 proportionally to cell elongation, demonstrating that cell growth alone is sufficient to drive nucleoid
329 segregation (Fig. 4I). However, rifampicin treatment also results in nucleoid expansion, causing increased
330 midcell DNA density when two nucleoids are present (Fig. 4G). Collectively, these findings show that
331 chromosome segregation progresses despite active ribosome dynamic and polysome dissociation while
332 the separation of daughter chromosomes is affected.

333 To compare these data to our model, we divide the rifampicin-treated cells into three age groups based on
334 their nucleoid segregation stages. This grouping was necessary because rifampicin treatment starts at
335 different cell cycle ages for the asynchronous cell population in Fig. 4. The first group, representing 12% of
336 cells, includes those cells where T_{min} was detected before treatment began ($T_{min} < T_{ab}$, $N = 92$) (SI Fig.
337 S12). The second group, comprising 17% of cells, includes cells in which nucleoid separation was detected
338 after treatment started ($T_{min} > T_{ab}$, $N = 138$). The largest group, accounting for 71% of cells ($N = 556$),

339 shows no detectable nucleoid separation either before or after treatment. Our following analysis focuses
340 on the first two groups, as the third group shows minimal changes in ribosome and nucleoid distributions
341 after the treatment. To model these two groups of cells, we set the polysome formation rate to zero at the
342 start of the treatment. We then evolve the model so that cell length changes the same way as in the
343 experiments (see Materials and Methods, *Rifampicin Treatment in the Model*, for details).

344 The group of cells that were late in their replication cycle at the onset of antibiotic treatment ($T_{min} < T_{ab}$),
345 show a local DNA density minimum (Fig. 5A) and a midcell ribosome accumulation at the start of rifampicin
346 treatment (Fig. 5B). The midcell ribosome accumulation vanishes within about 16 min from the start of the
347 treatment (Fig. 5B-C). The same occurs in the model, although at a faster rate (Fig. 5E-F). At the same
348 time, the model and the data qualitatively differ in how DNA distributions evolved. The experimental data
349 show that the midcell DNA density minimum persists, albeit becoming shallower over a 50-minute period,
350 before plateauing (Fig. 5A,C, SI Fig. S13A). In contrast, in the model, the two nucleoid masses merge so
351 that the local DNA density minimum at the midcell completely vanishes (Fig.5D,F, SI Fig. S13B-C). The
352 coupled DNA ribosome dynamics model is thus not able to explain the persistence of the experimentally
353 observed nucleoid minimum after treatment.

354 We next examine the second group of cells ($T_{min} > T_{ab}$) where the DNA density minimum develops after
355 the start of rifampicin treatment (Fig. 5G-I, SI Fig. S14A). Although the observed DNA density minimum is
356 small in this group, its presence also contradicts the active mRNA-ribosome dynamics model. In the model,
357 the midcell DNA density minimum does not form without active ribosome dynamics (Fig. 5J-L, SI Fig. S14B-
358 C). The lack of the minimum is a qualitative feature of the model, independent of parameter selection. This
359 results from the overdamped nature of diffusive processes. Once the driving force is removed, that is, the
360 formation of polysomes is halted, then the separation of two nucleoid lobes stops immediately (SI Fig.
361 S14B-C). The qualitative discrepancy between the model and the data for cells with $T_{min} > 0$ show that
362 active dynamics of mRNA and ribosomes is not responsible for DNA separation in this group of cells.

363

364 **Discussion**

365 **Active mRNA-ribosome dynamics**

366 This study provides both experimental and theoretical evidence supporting the role of active mRNA-
367 ribosome dynamics in the segregation and separation of chromosomal DNA in *E. coli* cells. A characteristic
368 feature of this mechanism, as also observed in our measurements (Fig. 2), is the accumulation of
369 polyribosomes (polysomes) at the nucleoid (and cell) center before it starts to split into two lobes. According
370 to our model, the accumulation of polyribosomes results from strong excluded volume interactions between
371 polysomes and chromosomal DNA (50), leading to the exclusion of DNA from the midcell region. These
372 qualitative features of the model are consistent with our data in steady-state growth conditions. Perturbative
373 measurements with rifampicin treatment furthermore show that the nucleoid split does not develop in the

374 majority of cells (77%) when polysome formation is inhibited due to the lack of mRNA substrates. However,
375 these measurements also show that in cells where nucleoid lobes have already formed at the start of the
376 treatment, the nucleoid centers continue to move apart as the cells continue to elongate (Fig. 4H, SI Fig.
377 S13C).

378 The latter finding indicates that the active mRNA-ribosome dynamics is not the sole process driving the late
379 segregation of nucleoids. Similar conclusions were recently reported by Papagiannakis *et al.,* although
380 based on different evidence (38). Notably, their measurements did not show further separation of nucleoid
381 lobes after the start of rifampicin treatment. This discrepancy likely arises from differences in growth
382 conditions between the two studies. Under faster growth rates, as used by Papagiannakis *et al.,* the cell
383 growth stops almost immediately after rifampicin treatment begins. In comparison, under the slower growth
384 conditions used in our study, cell growth continues for a considerable portion of time (more than 50 min in
385 our case). Accordingly, in faster growth conditions, further nucleoid lobe separation is not observed, given
386 that it is driven by continued cell elongation.

387 **Entropic mechanism**

388 What is the mechanism driving two nucleoid lobes apart in proportion to cell elongation, independent of
389 active mRNA-ribosome dynamics in the late stages of segregation? First, it can be ruled out that this
390 process is due to the passive macromolecular crowding, which remains present after rifampicin treatment.
391 Indeed, passive crowding without reactions could lead to aggregation of DNA at high crowding levels or
392 simply hinder DNA segregation and separation due to increased viscosity. Consistent with this view, a fusion
393 of nucleoids can be observed in *E. coli* cells treated with chloramphenicol (57), which stops protein
394 synthesis but not RNA synthesis. In this case, the high level of macromolecular crowding appears to result
395 from an increased level of RNA species (rRNA, tRNA, mRNA) in the cytosol (58). Alternatively, it has been
396 proposed that cell elongation could drive nucleoid segregation via transertion linkages (59). However, this
397 hypothesis can be ruled out by our rifampicin measurements because the linkages would disappear within
398 a few minutes from the start of the treatment, whereas the daughter nucleoids continue to move apart for a
399 much longer period (50 min).

400 At the same time, the cell elongation-dependent movement of nucleoid lobes apart can be consistent with
401 the entropic segregation mechanism (17,18,25). Polymer physics predicts that two daughter chromosomes,
402 under cylindrical confinement, will segregate from each other such that the center of each nucleoid remains
403 at the ¼ position of the cell, as long as two chromosomes remain in contact with each other (32). The
404 distance between the nucleoid centers, D_{peak} scales then proportional to cell length as observed in our
405 experiments. For the nucleoids to position exactly at the cell's ¼ positions the macromolecular crowding
406 effects need to be sufficiently weak so that each nucleoid fills half of the cell volume. This appears the case
407 in rifampicin treatment measurements. However, at stronger macromolecular crowding levels, the osmotic
408 pressure from crowders, can push two nucleoids together when there is no active mRNA-ribosome

409 dynamics in the end of the segregation phase. D_{peak} being proportional to L_{cell} then no longer holds. It is
410 unclear if the daughter nucleoids in normal growth conditions without rifampicin treatment experience weak
411 or strong crowding levels. We also emphasize that entropic mechanism is applicable only for the
412 segregation phase and it cannot explain any separation of two nucleoids.

413 **Constriction effect**

414 Our measurements also indicate that, in addition to active mRNA-ribosome dynamics a closing constriction
415 plays an important role in separating the two daughter nucleoids and partitioning them into daughter cell
416 compartments (Fig. 3). This likely occurs via steric interactions between the constriction and DNA. These
417 steric interactions could potentially be mediated by crowders, ensuring that the inner membrane and
418 chromosomal DNA do not come into direct contact. Interestingly, earlier research has shown that the onset
419 of constriction is blocked until DNA segregation has progressed to the point where there is a local DNA
420 density minimum at midcell /mid nucleoid (42). If the constriction were to start closing earlier, then it could
421 likely result in the trapping of incompletely replicated DNA under the constriction. Altogether, DNA
422 segregation to the point where there is a local DNA density minimum at the midcell appears to trigger the
423 onset of constriction, which completely separates one daughter chromosome from another. The
424 segregation process can thus be self-amplifying through the formation of the constriction.

425 **FtsK translocase**

426 Constriction, in the majority of cases, provides a faithful mechanism for partitioning the two chromosomes
427 to the daughter cells. When it fails and some DNA becomes trapped by the closing septum, then DNA
428 translocase FtsK (60,61) provides a last-resort mechanism to correct the error (31). FtsK usually acts on
429 about 400 kb region near the replication termination region around the *dif*-site (28) but it is capable of
430 directional pumping of more than 3 Mb of chromosomal DNA across closing constriction (31). This activity
431 mostly occurs at the very end of the constriction when the pore separating two daughters has a diameter
432 of less than 250 nm (31). The pore does not close fully until all the DNA is pumped across it. Altogether,
433 FtsK effectively guarantees a fail-safe completion of DNA partitioning. However, in most cell divisions, FtsK
434 is dispensable, as mutant cells are viable even when FtsK translocase activity has been inhibited (31,62).

435 **Integration**

436 In summary, our measurements and modeling, combined with findings from previous research, bring out
437 the involvement of several partially overlapping processes in the segregation and separation of daughter
438 chromosomes in *E. coli*. Based on these findings, we propose the following sequence of events unfolding
439 during the cell cycle (Fig. 6): The entropic mechanism is likely involved during the late segregation stage
440 when two chromosomes overlap (17,18). When about half of the DNA is replicated in slow growth
441 conditions, active mRNA-ribosome dynamics via excluded volume interactions become a sufficiently strong
442 driving force to lead to a midcell DNA density minimum. At this point, the entropic mechanism of segregation
443 still remains important, and, in fact, the associated force increases as more DNA is replicated (25,26).

However, the entropic force vanishes once two DNA molecules no longer overlap. In parallel, the formation of the midcell DNA density minimum via the active mRNA-ribosome dynamics triggers the onset of constriction in slow growth conditions (42). The constriction further drives the two daughter chromosomes apart and contributes to their separation. The final stages of DNA partitioning are further aided by FtsK if DNA becomes trapped by the closing constriction.

The involvement of active mRNA-ribosome dynamics in the segregation of the two DNA molecules in the process outlined above (Fig. 6) may appear to some degree redundant and may not be essential for partitioning the DNA molecules into daughter cells. However, this mechanism is inherently present in actively growing cells where gene expression takes place. Harnessing transcription and translation processes to accelerate DNA segregation offers a clear advantage, especially in growth conditions where DNA segregation is a limiting factor for the duration of the cell cycle (42,63).

Outlook and future directions

Further work is needed to validate the proposed processes outlined in Fig. 6. In particular, the existing evidence for the entropic mechanism remains indirect. Using synthetic cell systems implemented in microfluidic platforms, such as the genome-in-the-box (64) or minimal cells (65), will help further elucidate the role of this mechanism. An open question is also whether additional molecular systems beyond those listed in Fig. 6 are involved in the segregation and separation of chromosomal DNA in *E. coli*.

Significant effort is still required to develop models that can simulate these processes in sufficient detail, ideally integrating them into a single platform. For the active mRNA-ribosome dynamics models, it remains unclear to what degree the findings from 1D models apply in a 3D setting. Additionally, these reaction-diffusion models lack chain connectivity for DNA, which may alter the results. We hope the experimental evidence presented here motivates further computational efforts to address these gaps in our understanding.

Materials and Methods

Details of bacterial growth conditions, microchip design, fluorescence microscopy setup, and image analysis, and modeling are given in the SI Information, Materials and Methods. The list of all strains and plasmids used in this study, including their sources, is given in the SI Information, Table S1.

Acknowledgments

The authors thank Rachel McCord and Steve Abel for their valuable comments. A part of this research was conducted at the Center for Nanophase Materials Sciences, which is sponsored at Oak Ridge National Laboratory by the Scientific User Facilities Division, Office of Basic Energy Sciences, U.S. Department of Energy. This work was supported by the National Institutes of Health award GM127413 (JM) and NSF MCB2313719 (JM).

References

1. Bloom K, Joglekar A (2010) Towards building a chromosome segregation machine. *Nature* **463**:446-456. doi:10.1038/nature08912.
2. Wang X, Llopis PM, Rudner DZ (2013) Organization and segregation of bacterial chromosomes. *Nat. Rev. Genet.* **14**:191-203. doi:10.1038/nrg3375.
3. Gogou C, Japaridze A, Dekker C (2021) Mechanisms for chromosome segregation in bacteria. *Frontiers in Microbiology* **12**:685687. doi:10.3389/fmicb.2021.685687.
4. Batty P, Gerlich DW (2019) Mitotic chromosome mechanics: how cells segregate their genome. *Trends in Cell Biology* **29**:717-726. doi:10.1016/j.tcb.2019.05.007.
5. Woldringh CL, Hansen FG, Vischer NOE, Atlung T (2015) Segregation of chromosome arms in growing and non-growing *Escherichia coli* cells. *Frontiers in Microbiology.* **6**. doi:10.3389/fmicb.2015.00448.
6. Bates D, Kleckner N (2005) Chromosome and replisome dynamics in *E. coli*: Loss of sister cohesion triggers global chromosome movement and mediates chromosome segregation. *Cell* **121**:899-911. doi:10.1016/j.cell.2005.04.013.
7. Viollier PH, Thanbichler M, McGrath PT, West L, Meewan M, McAdams HH, Shapiro L (2004) Rapid and sequential movement of individual chromosomal loci to specific subcellular locations during bacterial DNA replication. *Proc. Natl. Acad. Sci. U. S. A.* **101**:9257-9262. doi:10.1073/pnas.0402606101.
8. Nielsen HJ, Ottesen JR, Youngren B, Austin SJ, Hansen FG (2006) The *Escherichia coli* chromosome is organized with the left and right chromosome arms in separate cell halves. *Mol. Microbiol.* **62**:331-338. doi:10.1111/j.1365-2958.2006.05346.x.
9. Cass JA, Kuwada NJ, Traxler B, Wiggins PA (2016) *Escherichia coli* chromosomal loci segregate from midcell with universal dynamics. *Biophys J* **110**:2597-2609. doi:10.1016/j.bpj.2016.04.046.
10. Badrinarayanan A, Le TBK, Laub MT (2015) Bacterial chromosome organization and segregation. *Annu Rev Cell Dev Biol* **31**:171-199. doi:10.1146/annurev-cellbio-100814-125211.
11. Lin DC, Grossman AD (1998) Identification and characterization of a bacterial chromosome partitioning site. *Cell* **92**:675-685. doi:10.1016/s0092-8674(00)81135-6.
12. Livny J, Yamaichi Y, Waldor MK (2007) Distribution of centromere-like parS sites in bacteria: insights from comparative genomics. *J Bacteriol* **189**:8693-8703. doi:10.1128/JB.01239-07.
13. Cornet F, Blanchais C, Dusfour-Castan R, Meunier A, Quebre V, Sekkouri Alaoui H, . . . Bouet JY (2023) DNA segregation in enterobacteria. *EcoSal Plus* **11**:eesp00382020. doi:10.1128/ecosalplus.esp-0038-2020.
14. Brahmachari S, Marko JF (2019) Chromosome disentanglement driven via optimal compaction of loop-extruded brush structures. *Proc. Natl. Acad. Sci. U. S. A.* **116**:24956-24965. doi:10.1073/pnas.1906355116.
15. Harju J, van Teeseling MCF, Broedersz CP (2024) Loop-extruders alter bacterial chromosome topology to direct entropic forces for segregation. *Nat Commun* **15**:4618. doi:10.1038/s41467-024-49039-w.
16. Makela J, Sherratt D (2020) SMC complexes organize the bacterial chromosome by lengthwise compaction. *Curr Genet* **66**:895-899. doi:10.1007/s00294-020-01076-w.

17. Jun S, Mulder B (2006) Entropy-driven spatial organization of highly confined polymers: lessons for the bacterial chromosome. *Proc. Natl. Acad. Sci. U. S. A.* **103**:12388-12393. doi:10.1073/pnas.0605305103

18. Jun S, Wright A (2010) Entropy as the driver of chromosome segregation. *Nat. Rev. Microbiol.* **8**:600-607. doi:10.1038/nrmicro2391

19. Jun S, Arnold A, Ha BY (2007) Confined space and effective interactions of multiple self-avoiding chains. *Phys. Rev. Lett.* **98**:128303. doi:10.1103/PhysRevLett.98.128303.

20. Jung Y, Ha BY (2010) Overlapping two self-avoiding polymers in a closed cylindrical pore: implications for chromosome segregation in a bacterial cell. *Phys. Rev. E* **82**:051926. doi:10.1103/PhysRevE.82.051926.

21. Liu Y, Chakraborty B (2012) Segregation of polymers in confined spaces. *Phys. Biol.* **9**:066005. doi:10.1088/1478-3975/9/6/066005.

22. Dorier J, Stasiak A (2013) Modelling of crowded polymers elucidate effects of double-strand breaks in topological domains of bacterial chromosomes. *Nucleic Acids Res.* **41**:6808-6815. doi:10.1093/nar/gkt480.

23. Shin J, Cherstvy AG, Metzler R (2014) Mixing and segregation of ring polymers: spatial confinement and molecular crowding effects. *New Journal of Physics* **16**:053047. doi:10.1088/1367-2630/16/5/053047.

24. Chen YH, Yu WC, Wang JJ, Luo KF (2015) Polymer segregation under confinement: Influences of macromolecular crowding and the interaction between the polymer and crowders. *J. Chem. Phys.* **143**:134904. doi:10.1063/1.4932370.

25. Männik J, Castillo D, Yang D, Siopsis G, Männik J (2016) The role of MatP, ZapA, and ZapB in chromosomal organization and dynamics in *Escherichia coli*. *Nucleic Acids Res.* **44**:1216-1226. doi:10.1093/nar/gkv1484.

26. Polson JM, Kerry DRM (2018) Segregation of polymers under cylindrical confinement: effects of polymer topology and crowding. *Soft Matter* **14**:6360-6373. doi:10.1039/c8sm01062e.

27. Männik J, Bailey MW (2015) Spatial coordination between chromosomes and cell division proteins in *Escherichia coli*. *Frontiers in Microbiology* **6**:306. doi:10.3389/fmicb.2015.00306.

28. Stouf M, Meile J-C, Cornet F (2013) FtsK actively segregates sister chromosomes in *Escherichia coli*. *Proc. Natl. Acad. Sci. U. S. A.* **110**:11157-11162. doi:10.1073/pnas.1304080110.

29. Galli E, Midonet C, Paly E, Barre FX (2017) Fast growth conditions uncouple the final stages of chromosome segregation and cell division in *Escherichia coli*. *PLoS Genet.* **13**:1006702. doi:10.1371/journal.pgen.1006702.

30. Barre FX, Aroyo M, Colloms SD, Helfrich A, Cornet F, Sherratt DJ (2000) FtsK functions in the processing of a Holliday junction intermediate during bacterial chromosome segregation. *Genes Dev.* **14**:2976-2988. doi:10.1101/gad.188700.

31. Männik J, Bailey MW, O'Neill JC, Männik J (2017) Kinetics of large-scale chromosomal movement during asymmetric cell division in *Escherichia coli*. *PLoS Genet.* **13**:e1006638. doi:10.1371/journal.pgen.1006638.

32. Wu FB, Swain P, Kuijpers L, Zheng X, Felter K, Guurink M, . . . Dekker C (2019) Cell boundary confinement sets the size and position of the *E. coli* chromosome. *Curr. Biol.* **29**:2131-2144. doi:10.1016/j.cub.2019.05.015.

33. Miangolarra AM, Li SHJ, Joanny JF, Wingreen NS, Castellana M (2021) Steric interactions and out-of-equilibrium processes control the internal organization of bacteria. *Proc. Natl. Acad. Sci. U. S. A.* **118**: e2106014118. doi:10.1073/pnas.2106014118.

34. Sanamrad A, Persson F, Lundius EG, Fange D, Gynna AH, Elf J (2014) Single-particle tracking reveals that free ribosomal subunits are not excluded from the *Escherichia coli* nucleoid. *Proc. Natl. Acad. Sci. U. S. A.* **111**:11413-11418. doi:10.1073/pnas.1411558111.

35. Mohapatra S, Weisshaar JC (2018) Functional mapping of the *E. coli* translational machinery using single-molecule tracking. *Mol. Microbiol.* **110**:262-282. doi:10.1111/mmi.14103.

36. Youngren B, Nielsen HJ, Jun S, Austin S (2014) The multifork *Escherichia coli* chromosome is a self-duplicating and self-segregating thermodynamic ring polymer. *Genes Dev.* **28**:71-84. doi:10.1101/gad.231050.113.

37. Makela J, Uphoff S, Sherratt DJ (2021) Nonrandom segregation of sister chromosomes by *Escherichia coli* MukBEF. *Proc. Natl. Acad. Sci. U. S. A.* **118**:e2022078118. doi:10.1073/pnas.2022078118.

38. Papagiannakis A, Yu Q, Govers SK, Lin W-H, Wingreen NS, Jacobs-Wagner C (2025) DNA/polysome phase separation and cell width confinement couple nucleoid segregation to cell growth in *Escherichia coli*. doi:10.7554/elife.104276.1.

39. Sadhir I, Murray SM (2023) Mid-cell migration of the chromosomal terminus is coupled to origin segregation in Escherichia coli. *Nat Commun* **14**:7489. doi:10.1038/s41467-023-43351-7.

40. Reyes-Lamothe R, Sherratt DJ, Leake MC (2010) Stoichiometry and architecture of active DNA replication machinery in *Escherichia coli*. *Science* **328**:498-501.

41. Wery M, Woldringh CL, Rouviere-Yaniv J (2001) HU-GFP and DAPI co-localize on the *Escherichia coli* nucleoid. *Biochimie* **83**:193-200.

42. Tiruvadi-Krishnan S, Männik J, Kar P, Lin J, Amir A, Männik J (2022) Coupling between DNA replication, segregation, and the onset of constriction in *Escherichia coli*. *Cell Reports* **38**:110539. doi:10.1016/j.celrep.2022.110539.

43. Wang P, Robert L, Pelletier J, Dang WL, Taddei F, Wright A, Jun S (2010) Robust growth of *Escherichia coli*. *Curr. Biol.* **20**:1099-1103.

44. Yang D, Jennings AD, Borrego E, Retterer ST, Männik J (2018) Analysis of factors limiting bacterial growth in PDMS mother machine devices. *Frontiers in Microbiology* **9**:871. doi:10.3389/fmicb.2018.00871.

45. Yang D, Männik J, Retterer ST, Männik J (2020) The effects of polydisperse crowders on the compaction of the *Escherichia coli* nucleoid. *Mol Microbiol* **113**:1022-1037. doi:10.1111/mmi.14467.

46. Gray WT, Govers SK, Xiang YJ, Parry BR, Campos M, Kim S, Jacobs-Wagner C (2019) Nucleoid size scaling and intracellular organization of translation across bacteria. *Cell* **177**:1632-1648. doi:10.1016/j.cell.2019.05.017.

47. Bakshi S, Choi H, Mondal J, Weisshaar JC (2014) Time-dependent effects of transcription- and translation-halting drugs on the spatial distributions of the *Escherichia coli* chromosome and ribosomes. *Mol. Microbiol.* **94**:871-887. doi:10.1111/mmi.12805.

48. Bakshi S, Siryaporn A, Goulian M, Weisshaar JC (2012) Superresolution imaging of ribosomes and RNA polymerase in live *Escherichia coli* cells. *Mol. Microbiol.* **85**:21-38. doi:10.1111/j.1365-2958.2012.08081.x.

49. Mondal J, Bratton BP, Li YJ, Yethiraj A, Weisshaar JC (2011) Entropy-based mechanism of ribosome-nucleoid segregation in *E. coli* cells. *Biophys. J.* **100**:2605-2613. doi:10.1016/j.bpj.2011.04.030.

50. Chang MH, Lavrentovich MO, Mannik J (2024) Differentiating the roles of proteins and polysomes in nucleoid size homeostasis in *Escherichia coli*. *Biophys J* **123**:1. doi:10.1016/j.bpj.2023.11.010.

51. Chai Q, Singh B, Peisker K, Metzendorf N, Ge XL, Dasgupta S, Sanyal S (2014) Organization of ribosomes and nucleoids in *Escherichia coli* cells during growth and in quiescence. *Journal of Biological Chemistry* **289**:11342-11352. doi:10.1074/jbc.M114.557348.

52. Cunha S, Woldringh CL, Odijk T (2001) Polymer-mediated compaction and internal dynamics of isolated *Escherichia coli* nucleoids. *J. Struct. Biol.* **136**:53-66. doi:10.1006/jsbi.2001.4420.

53. Gelber I, Aranovich A, Feingold M, Fishov I (2021) Stochastic nucleoid segregation dynamics as a source of the phenotypic variability in *E. coli*. *Biophys. J.* **120**:5107-5123. doi:10.1016/j.bpj.2021.10.004.

54. Yu XC, Tran AH, Sun Q, Margolin W (1998) Localization of cell division protein FtsK to the Escherichia coli septum and identification of a potential N-terminal targeting domain. *J Bacteriol* **180**:1296-1304. doi:10.1128/JB.180.5.1296-1304.1998.

55. Wlodarski M, Raciti B, Kotar J, Cosentino Lagomarsino M, Fraser GM, Cicuta P (2017) Both genome and cytosol dynamics change in *E. coli* challenged with sublethal rifampicin. *Phys Biol* **14**:015005. doi:10.1088/1478-3975/aa5b71.

56. Bernstein JA, Khodursky AB, Lin PH, Lin-Chao S, Cohen SN (2002) Global analysis of mRNA decay and abundance in Escherichia coli at single-gene resolution using two-color fluorescent DNA microarrays. *Proc. Natl. Acad. Sci. U. S. A.* **99**:9697-9702. doi:10.1073/pnas.112318199.

57. Van Helvoort J, Huls PG, Vischer NOE, Woldringh CL (1998) Fused nucleoids resegregate faster than cell elongation in *Escherichia coli* pbpB(Ts) filaments after release from chloramphenicol inhibition. *Microbiology* **144**:1309-1317. doi:10.1099/00221287-144-5-1309.

58. Xiang YJ, Surovtsev IV, Chang YJ, Govers SK, Parry BR, Liu J, Jacobs-Wagner C (2021) Interconnecting solvent quality, transcription, and chromosome folding in *Escherichia coli*. *Cell* **184**:3626-3642. doi:10.1016/j.cell.2021.05.037.

59. Woldringh CL (2002) The role of co-transcriptional translation and protein translocation (transertion) in bacterial chromosome segregation. *Mol. Microbiol.* **45**:17-29. doi:10.1046/j.1365-2958.2002.02993.x.

60. Demarre G, Galli E, Barre FX (2013) The FtsK family of DNA pumps. *Adv Exp Med Biol* **767**:245-262. doi:10.1007/978-1-4614-5037-5_12.

61. Besprozvannaya M, Burton BM (2014) Do the same traffic rules apply? Directional chromosome segregation by SpoIIIE and FtsK. *Mol. Microbiol.* **93**:599-608. doi:10.1111/mmi.12708.

62. Kennedy SP, Chevalier F, Barre F-X (2008) Delayed activation of Xer recombination at *dif* by FtsK during septum assembly in *Escherichia coli*. *Mol. Microbiol.* **68**:1018-1028. doi:10.1111/j.1365-2958.2008.06212.x.

63. Micali G, Grilli J, Marchi J, Osella M, Lagomarsino MC (2018) Dissecting the control mechanisms for DNA replication and cell division in *E. coli*. *Cell Reports* **25**:761-771. doi:10.1016/j.celrep.2018.09.061.

64. Birnie A, Dekker C (2021) Genome-in-a-box: building a chromosome from the bottom up. *ACS Nano* **15**:111-124. doi:10.1021/acsnano.0c07397.

65. Gibson DG, Glass JI, Lartigue C, Noskov VN, Chuang RY, Algire MA, . . . Venter JC (2010) Creation of a bacterial cell controlled by a chemically synthesized genome. *Science* **329**:52.

Figures

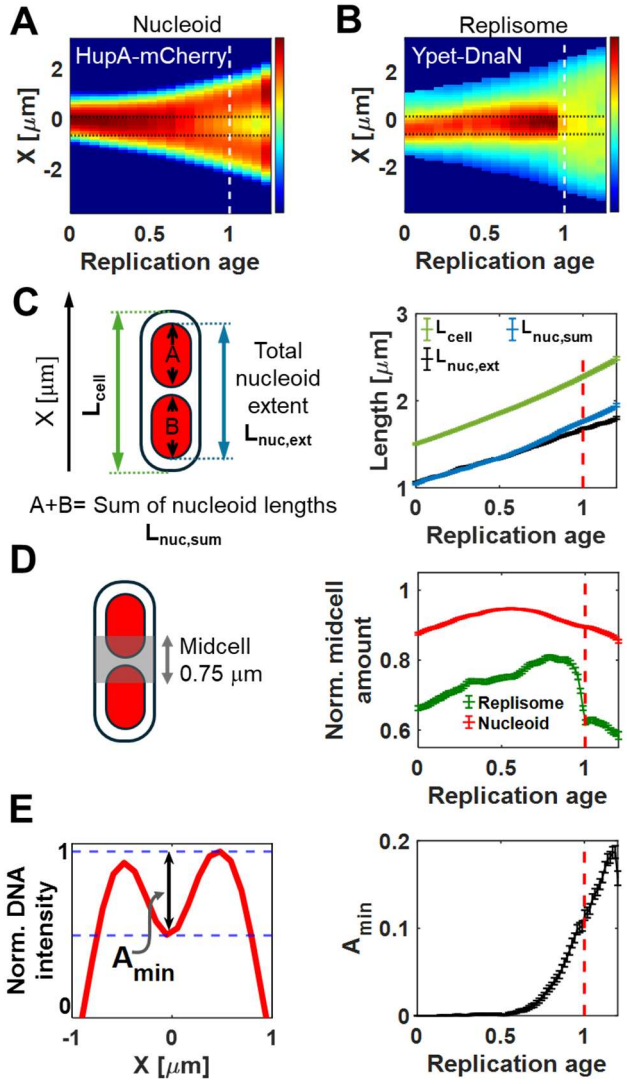

Fig. 1. Segregation of nucleoids as a function of DNA replication time (age). (A) The population average DNA density distribution along the long axis of the cell as a function of replication cycle age. Time zero corresponds to replication initiation and one to termination (also indicated by a vertical dashed line). HupA-mCherry labeling is used to infer DNA density distribution. Red corresponds to high- and blue to low-intensity values. The dashed horizontal lines indicate a midcell region. (B) The same for the average replisome density distribution. Ypet-DnaN labeling is used to infer this distribution. (C) Left: definition of parameters characterizing the dimensions of nucleoids: $L_{nuc,sum}$ and $L_{nuc,ext}$. Right: change of cell length L_{cell}, $L_{nuc,sum}$ and $L_{nuc,ext}$ as a function of replication cycle time. The dashed vertical line marks replication termination. (D) Left: schematics showing the region where HupA-mCherry and Ypet-DnaN midcell amount is measured (indicated also by the horizontal dashed lines in panels A and B). The midcell amount is based on the integrated intensity of fluorescent labels in this band. Right: the normalized midcell

amount for nucleoid (red) and replisome (green) as a function of replication age. The curves for individual cells are normalized by the maximum value during the whole measurement period and then averaged over the cell population. (E) Left: schematics showing the DNA density distribution for a single cell at a single time point and how the depth of the local minimum, A_{min}, is defined. Right: A_{min} as a replication cycle time. Error bars in panels C-E are s.e.m. N=438

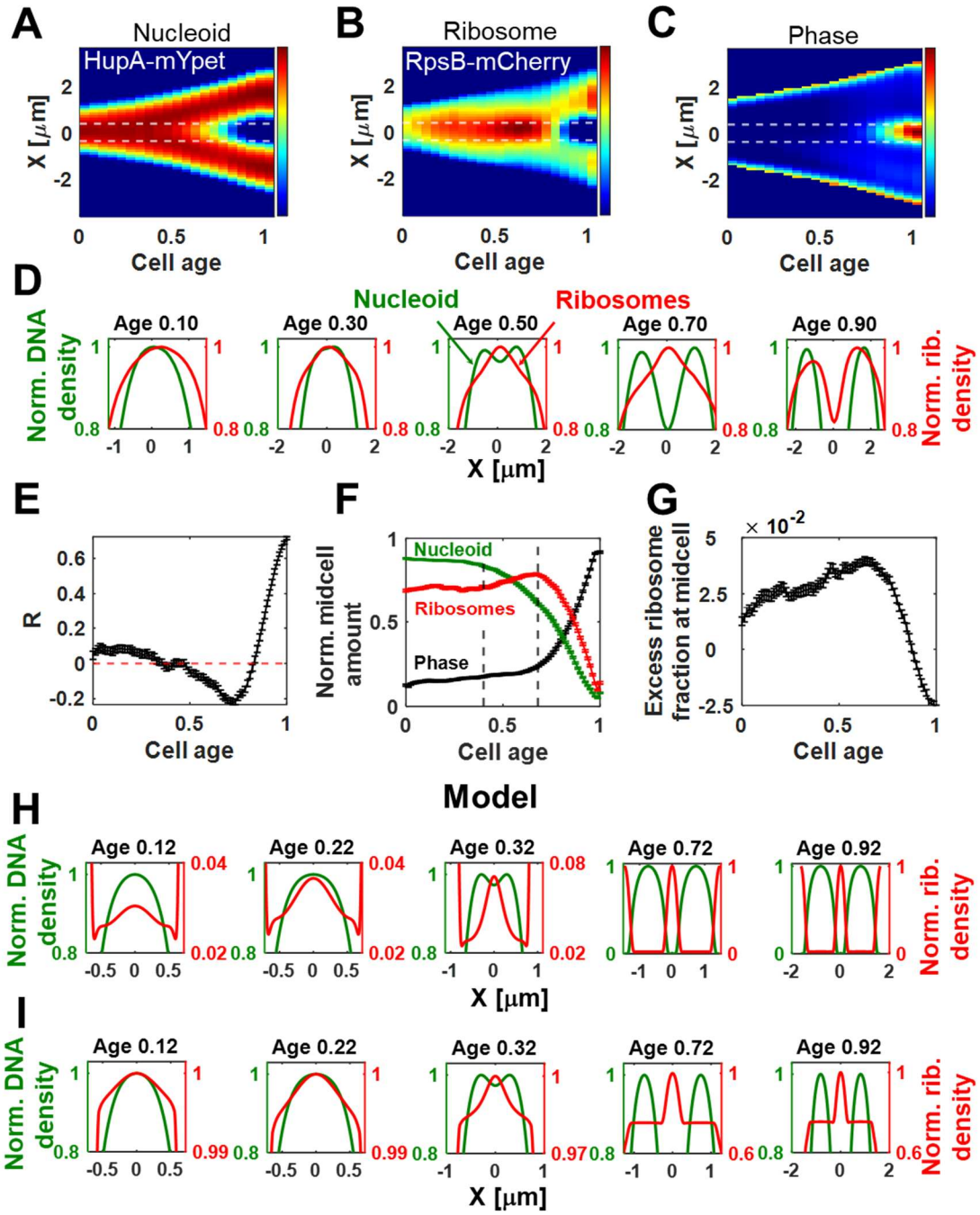

Figure 2. Cell-cycle dependent changes in DNA and ribosome density distributions and their comparison to model predictions. (A) Population averaged kymograph of DNA density distribution (HupA-mYpet) along the long axis of the cell as a function of cell age. Zero corresponds to cell birth and one to division. Red corresponds to high- and blue to low-intensity values. The dashed horizontal lines indicate a midcell region. (B) The same for ribosome density (RpsB-mCherry) distribution. (C) Phase contrast kymograph for the same cell population. (D) The normalized population-averaged density of nucleoid (green) and ribosomes

502 (red) along the long axis of the cell at different cell ages. The curves are normalized by their peak values.
503 (E) Pearson correlation coefficient, R, between nucleoid and ribosome densities as a function of cell age.
504 The coefficient is averaged over the cell population at each cell age point. (F) The integrated intensity within
505 the 0.75 μm wide band around the cell middle is shown for the nucleoid (green), ribosome (red) and phase
506 contrast signals (black). The curves from individual cells are normalized by their peak values and then
507 averaged over the cell population. The left vertical dashed line corresponds to cell age of 0.40 and the right
508 one to 0.68. (G) The relative excess fraction of ribosomes in the midcell band as a function of cell cycle
509 time. The curve is derived from a fitting of the ribosome signal (see Methods). N=486 for panels A-G. The
510 error bars are s.e.m. for panels E-G. (H) The normalized DNA and ribosome densities along the long axis
511 of the cell at different cell ages, as predicted by the coupled DNA and ribosome dynamics model. The
512 curves are normalized by their peak values. Note that the DNA (left) and ribosome (right) signals have
513 different scales, and the cell ages are comparable but not identical as those in panel D. (I) The same curves
514 that are recalculated, assuming a concentric shell of ribosomes around the nucleoid (for details, see the
515 Concentric Shell Model in Methods). The shell's inner radius is 0.5×R_{cell}.

516

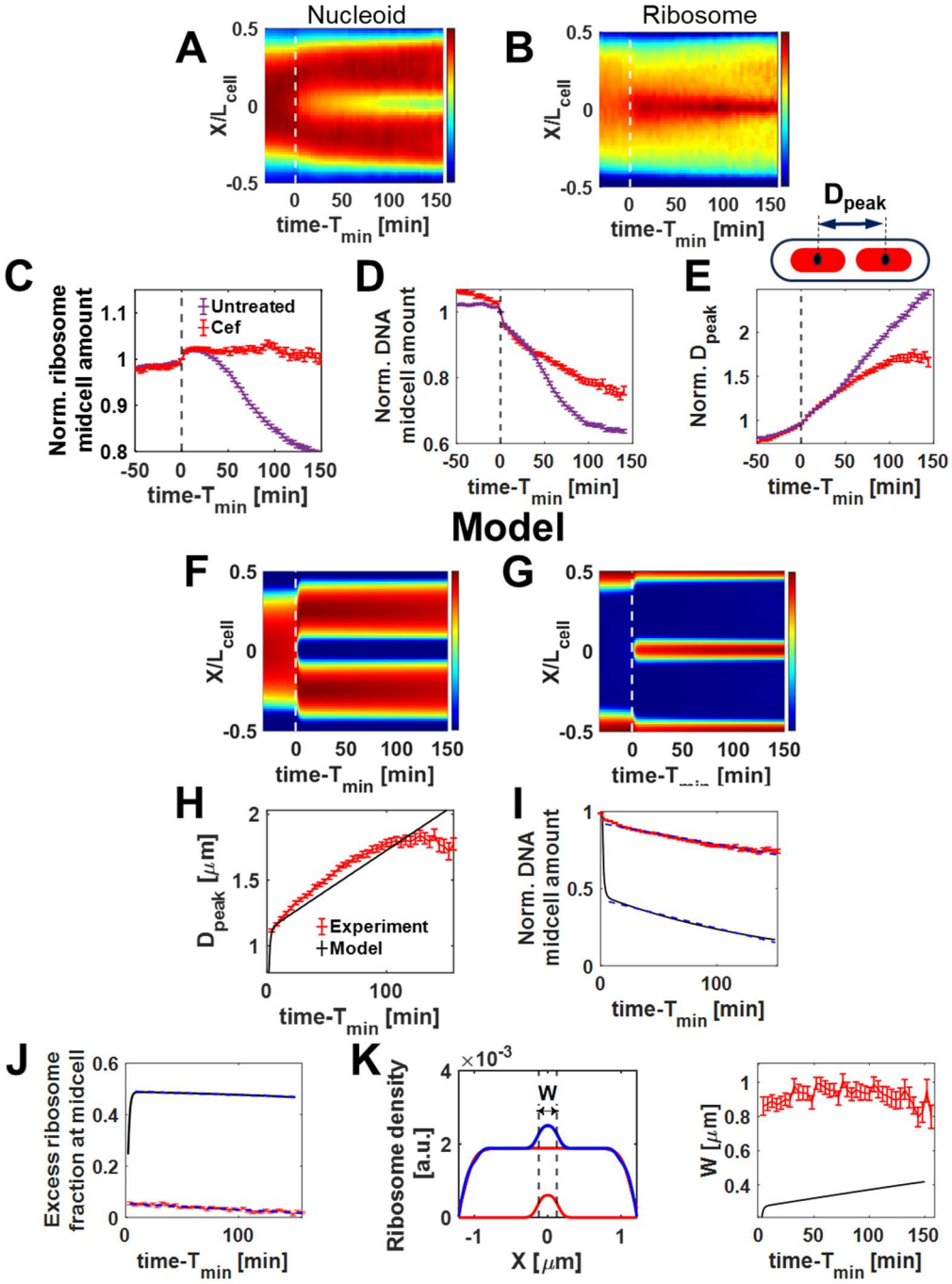

Figure 3. Segregation of nucleoids with and without closing constriction. (A) A population-averaged kymograph of DNA density along the long axis of the cell as a function of absolute (unscaled) time from the formation of local DNA density minimum, T_{min}, for cephalexin-treated non-constricting cells. The vertical axis shows normalized cell length, which remains unchanged throughout the experiment. Note that cells filament in this measurement. (B) The same for ribosome density distribution in this cell population. (C) The

average number of ribosomes at midcell as a function of time from T_{min} for cephalexin-treated (red) and untreated cells (violet). The curves are normalized so that the amounts are one at time T_{min}. (D) The normalized DNA amount at midcell is presented the same way as in the previous panel. (E) The average distance between nucleoid centers (peak distance) as a function of time from T_{min} for cephalexin-treated (red) and untreated cells (violet). The distances are normalized at T_{min}. The schematic on the top shows how the peak distance is defined. (F) Kymograph of nucleoid density from the coupled DNA and ribosome dynamics model presented the same way as the experimental data in panel A. (G) Kymograph of ribosome density from the model. (H) The peak distance as a function of time relative to T_{min} from cephalexin-treated cells (red) and from the model (black). (I) Normalized midcell DNA amount for cephalexin-treated cells (red) and model (black). The linear fits to both curves are shown by dashed lines. The model is fitted for $\mathrm{time} - T_{min} > 5\ \mathrm{min}$. (J) The relative excess fraction of ribosomes at midcell for cephalexin-treated cells (red) and model (black). The linear fits for both curves are shown as dashed blue lines. The fit coefficients for panels I and J are listed in Table S3. (K) Left: Schematic showing how the width of the midcell accumulation of ribosomes, W, is determined based on ribosome density profile (blue) and it's fit by generalized Gaussian curves (red). Right: the time evolution of W for cephalexin-treated cells (red) and the model (black). All error bars are s.e.m. N=235.

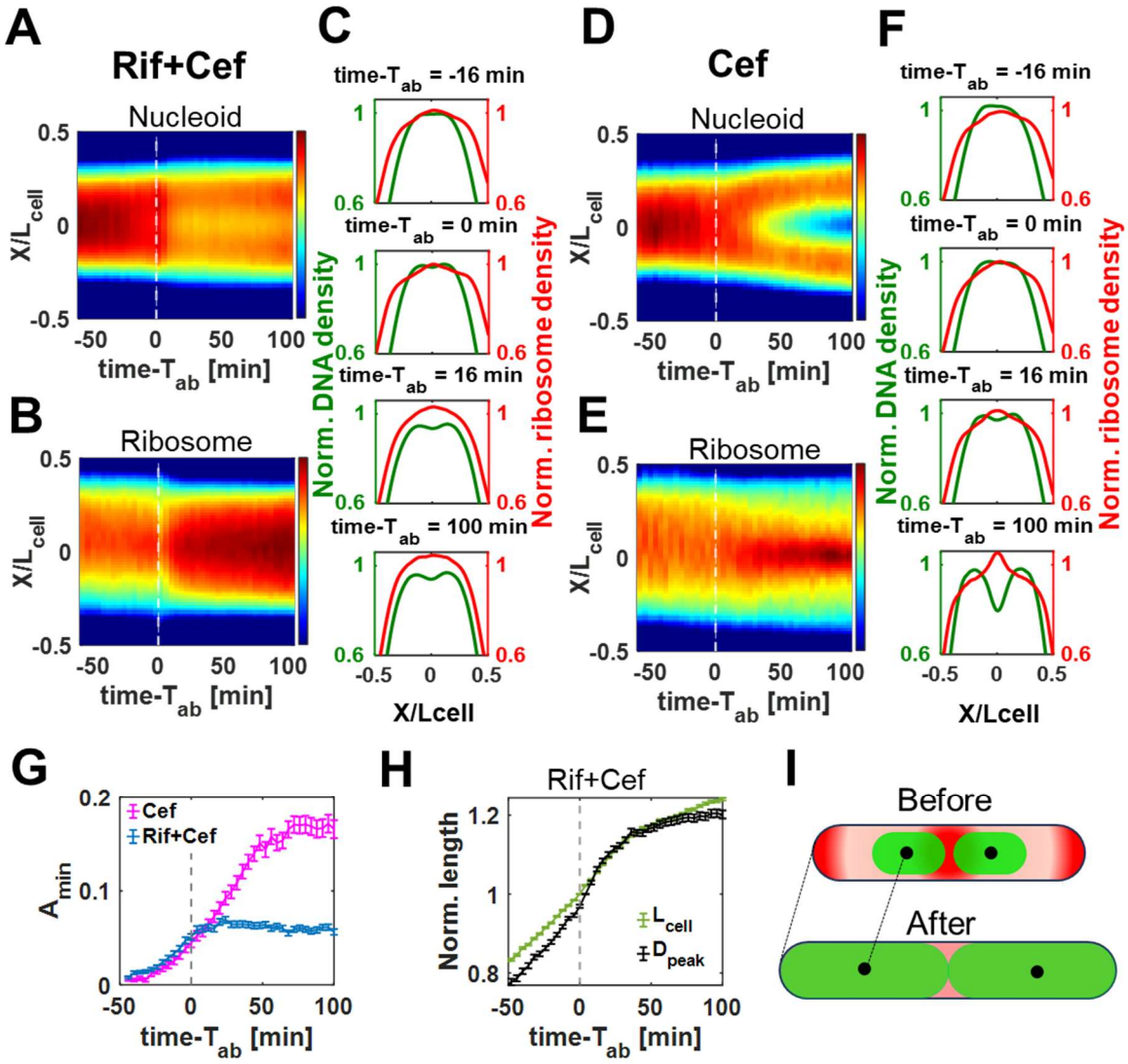

Figure 4. The effects from the disruption of active mRNA-polysome dynamics with rifampicin (Rif) on nucleoid and ribosome distributions. (A, D) The population-averaged kymographs of DNA density. The times are relative to the start of antibiotic treatment, T_{ab}, with Rif and Cef (cephalexin), and with only Cef, respectively. All analyzed cells in this figure are non-constricting. (B, E) The same for the average ribosome density. (C, F) The density distributions of DNA (green) and ribosome (red) along the long axis of the cell at different time points. In all panels, the curves are normalized relative to their maximum value at T_{ab}. (G) The depth of the local DNA density minimum at midcell as a function of time relative to the start of antibiotic treatment with Rif + Cef (blue) and Cef only (pink). (H) The average cell length (green) and the nucleoid peak distance (black) as a function of time from the start of the treatment for Rif + Cef treated cells. The curves from individual cells are normalized to one at T_{ab}. Error bars in panels G and H are s.e.m. (I) Schematic summarizing the expansion and movement of nucleoids and ribosomes during Rif treatment.

The top corresponds to a cell just before and bottom after Rif (+Cef) treatment. $N = 786$ for Rif+Cef and $N = 310$ for only Cef treated cells.

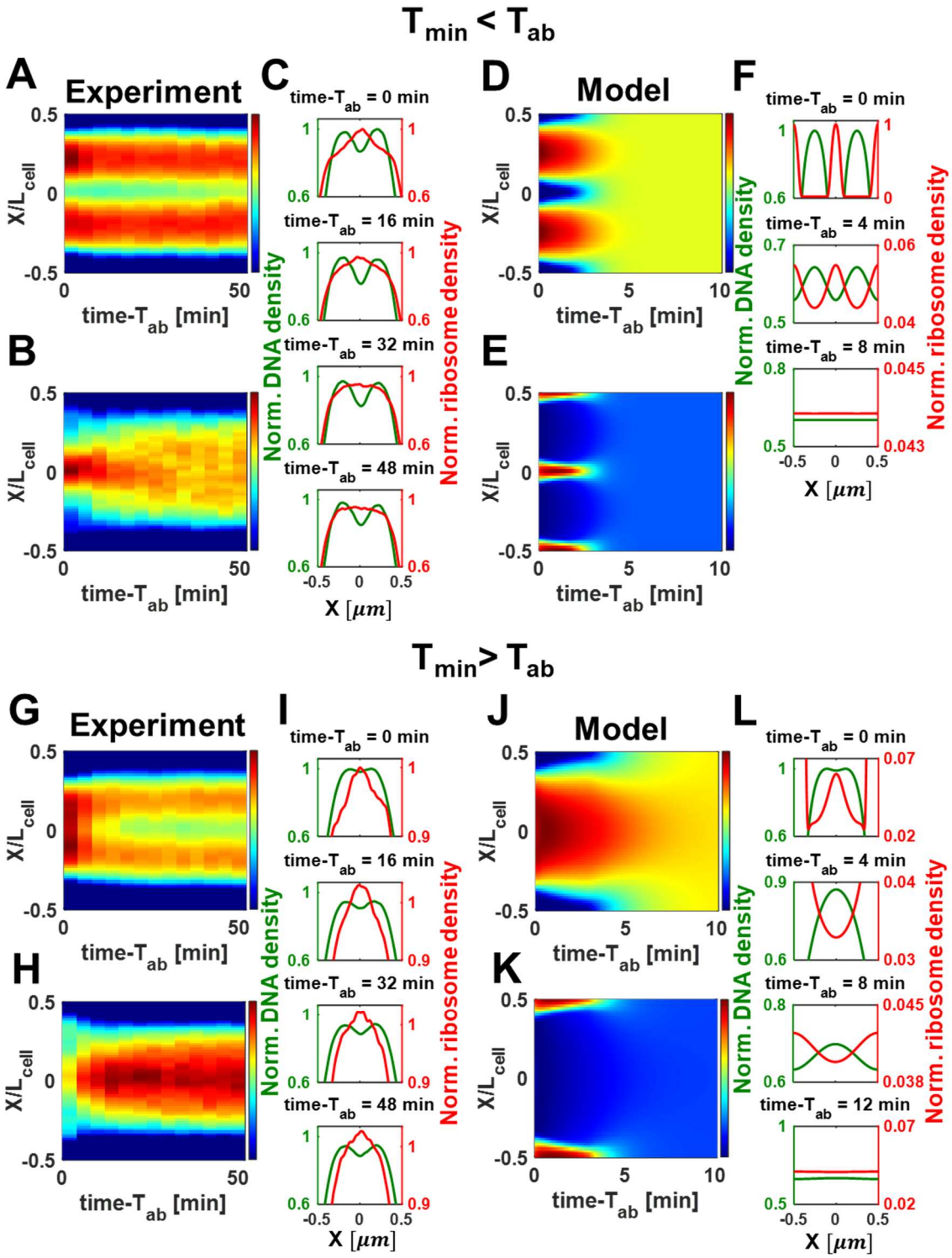

556

557 **Figure 5.** Comparing DNA and ribosome dynamics in Rif+Cef treated cells to the coupled DNA and
558 ribosome dynamics model. Cells from two age groups are compared. (A-F) Data and model for cells that
559 have formed a local DNA density minimum before the antibiotic treatment, $T_{min} < T_{ab}$ ($N = 92$). (A, B) The
560 kymographs of DNA and ribosome density, respectively. The times are relative to the start of antibiotic

561 treatment. (C) The average DNA (green) and ribosome (red) distributions along the long axis of the cell at
562 different time points of experiment. (D, E) The DNA and ribosome density kymographs, respectively, from
563 the model corresponding to group of cells with $T_{min} < T_{ab}$. The cell length in the beginning of the treatment
564 is 2.87 μm. Note shorter times in the model compared to experimental data. (F) The average DNA (green)
565 and ribosome (red) distributions along the long axis of the cell at different time points from the model. (G-
566 L) Data and model for cells that formed a local DNA density minimum after the start of the antibiotic
567 treatment, $T_{min} > T_{ab}$ ($N = 138$). (G,H) The kymographs of DNA and ribosome density, respectively. (I) The
568 average DNA (green) and ribosome (red) distributions along the long axis of the cell at different time points
569 of the experiment. (J, K) The DNA and ribosome density kymographs, respectively, from the model
570 corresponding to group of cells with $T_{min} > T_{ab}$. The cell length in the beginning of the treatment is 2.24 μm.
571 Note shorter times in the model compared to experimental data. (F) The average DNA (green) and
572 ribosome (red) distributions along the long axis of the cell at different time points from the model.

573

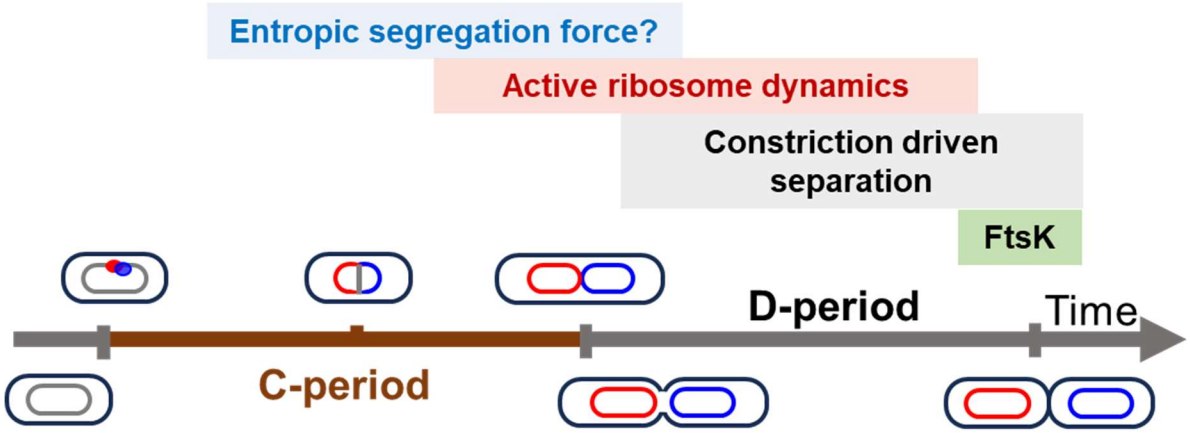

Figure 6. Progression of different mechanisms involved in segregation and separation of daughter chromosomes during *E. coli* cell cycle. The schematic summarizes the results from this work and from previously published studies. C-period marks the replication period, and D-period marks the duration from the termination of DNA replication to the final division of two daughter cells. The drawn schematic corresponds to slow growth conditions where the replication initiates after cell birth.